

Field-effect transistors and intrinsic mobility in ultra-thin MoSe₂ layers

S. Larentis, B. Fallahzad, and E. Tutuc

*Microelectronics Research Center, Department of Electrical and Computer Engineering,
The University of Texas at Austin, Austin, TX78758, USA*

We report the fabrication of back-gated field-effect transistors (FETs) using ultra-thin, mechanically exfoliated MoSe₂ flakes. The MoSe₂ FETs are *n*-type and possess a high gate modulation, with On/Off ratios larger than 10⁶. The devices show asymmetric characteristics upon swapping the source and drain, a finding explained by the presence of Schottky barriers at the metal contact/MoSe₂ interface. Using four-point, back-gated devices we measure the intrinsic conductivity and mobility of MoSe₂ as a function of gate bias, and temperature. Samples with a room temperature mobility of ~50 cm²/V·s show a strong temperature dependence, suggesting phonons are a dominant scattering mechanism.

Transition metal dichalcogenides (TMDs) are materials characterized by a MX₂ formula where M stands for a transition metal (Mo, W), and X stands for a chalcogen (S, Se or Te)^{1,2}. The transition metal dichalcogenides are layered materials, consisting of layers with an X-M-X structure. Within each layer the M-X bonds are covalent, while separate layers are bonded via Van der Waals interaction. Recent studies³⁻⁶ proved that micromechanical exfoliation, employed to isolate graphene monolayers⁷ is also an effective method to obtain thin flakes of various TMDs. The layers can be identified⁴⁻⁶ using optical microscope thanks to the thickness dependent contrast on SiO₂/Si substrates. Various TMD-based electronic devices have been demonstrated, with MoS₂ being investigated most extensively to date. Examples include MoS₂ monolayer *n*-type field effect transistors (FETs)^{8,9}, MoS₂ phototransistor¹⁰, MoS₂ bilayers chemical sensors¹¹, logic gates, memory cells and amplifiers using large MoS₂ flakes¹²⁻¹⁴. In addition, top-gated *p*-type FETs using monolayer WS₂¹⁵, and ambipolar back-gated FETs using multilayered WS₂¹⁶ have been demonstrated. The TMD-based FETs generally possess a high On/Off ratio, larger than 10⁵. Such semiconductors can be scaled down to a 0.7 nm thickness monolayer, which renders them attractive as an ultra-thin body for aggressively scaled FETs. The larger band-gap by comparison to graphene can ensure a large On/Off ratio.

In this study we examine the electron transport in another TMD, namely MoSe₂, a semiconductor with an indirect band-gap of 1.1 eV^{17,18} in bulk, which increase to 1.55 eV and become direct in monolayer and bilayer^{18,19}. We discuss the realization of field-effect transistors using ultrathin MoSe₂ flakes mechanically exfoliated on SiO₂/Si substrates. The MoSe₂ FETs are *n*-type, and possess a good gate control, with On/Off ratios larger than 10⁶. Four-point, gated devices allow us to measure the intrinsic conductivity, and extract the mobility of MoSe₂. The temperature (*T*) dependence reveals that the mobility increases significantly with decreasing the temperature, suggesting that phonon scattering dominates at room temperature.

The MoSe₂ flakes used here are produced by micromechanical exfoliation using commercially available MoSe₂ powder (Materion Inc.) with grain size < 44 μm (mesh -325). The MoSe₂ flakes are exfoliated on a 285 nm-thick SiO₂ film, thermally grown on highly doped *n*-type Si

(100) wafers ($N_D > 10^{20}$ cm⁻³). The exfoliated flakes are identified using optical microscope, and their thickness measured by atomic force microscopy (AFM). Figure 1(a) shows an optical micrograph of a MoSe₂ flake on SiO₂/Si substrate, while Fig. 1(b) shows the flake topography, probed by AFM, illustrating layered stacking. The typical flake size is 1-3 μm, and their thickness ranges between 3 to 80 nm. Individual MoSe₂ flakes typically exhibit terraces with various thicknesses, with a terrace surface roughness ranging from 0.2 to 0.6 nm. The optical contrast of the MoSe₂ on 285 nm thick SiO₂ substrate allows identification of flakes as thin as 4.8 nm (7 layers)⁴⁻⁶.

To assess the MoSe₂ quality we performed X-ray diffraction (XRD) on powder samples. The power XRD pattern, shown in Fig. 1(c) matches with the 2H-Dryadallite patterns²⁰ ensuring our material is characterized by hexagonal 2H-MoSe₂ structure with space group D_{6h}⁴ (P6₃/mmc)²¹, and in agreement with previous MoSe₂ powder XRDs^{22,23} studies. The full width at half maximum (FWHM) of the <002> peak is 0.223°. To further assess the exfoliated MoSe₂ flakes we performed μ-Raman spectroscopy using a Renishaw InVia Raman microscope. Figure 1(d-e) show Raman spectra using 442 nm [Fig. 1(d)] and 532 nm [Fig. 1(e)] excitation wavelengths on a MoSe₂ flake. The spectrum of Fig. 1(d), acquired with an incident laser power of 30 mW and 650 nm spot size presents four peaks at 169, 242, 285 and 352 cm⁻¹, corresponding to the E_{1g}, A_{1g}, E_{2g}¹ and A_{2u}² modes respectively, as reported by Sekine *et al.*²⁴ and more recently by Tongay *et al.*¹⁸. We note that the A_{2u}² mode (352 cm⁻¹) is an infrared active mode, not present in Raman scattering in bulk samples. The emergence of this mode in Raman scattering acquired on small flakes suggests a breakdown of inversion symmetry, possibly because of the substrate. A similar observation has been made recently in a Raman spectroscopy study of Bi₂Te₃ nanoplates²⁵. The Raman spectrum of Fig. 1(e), acquired with a 5 mW incident laser power shows similar peaks as Fig. 1(d) data, but with a higher intensity of the A_{1g} peak (242 cm⁻¹) with respect to the other modes. This observation is consistent with previous studies which show that the A_{1g} mode is better resolved at longer excitation wavelengths.²⁴

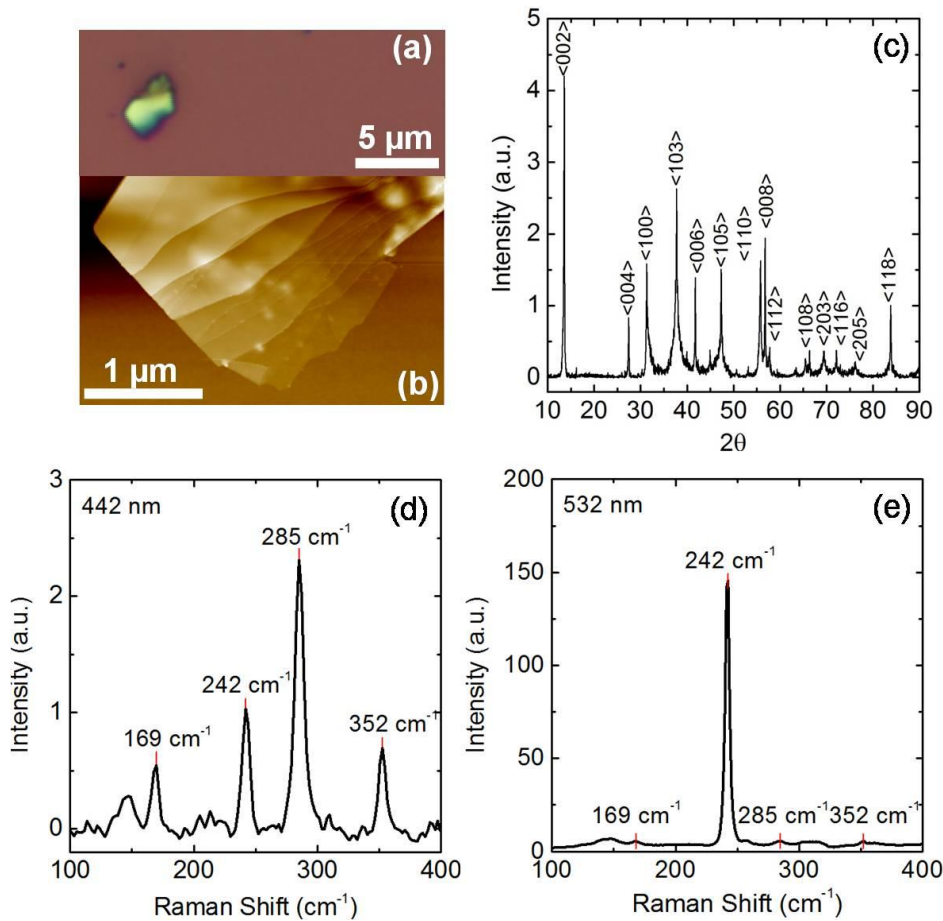


Fig. 1. (color online) (a) Optical micrograph of a MoSe₂ flake on SiO₂/Si substrate. (b) AFM topography of the thinner section (darker section in the optical image) of the same flake shown in panel (a). The data illustrates layered stacking in MoSe₂ flakes. (c) MoSe₂ powder XRD data. (d-e) Raman spectra acquired on a MoSe₂ flake using excitation wavelengths of 442 nm [panel (d)] and 532 nm [panel (e)].

The FWHM of E_{1g}, A_{1g}, E_{2g}¹ and A_{2u}² Raman peaks of Fig. 1(d) are 5.5, 5.2, 7, and 5 cm⁻¹ respectively. The A_{1g} peak FWHM of Fig. 1(e) is 3.5 cm⁻¹, assuming in all cases a Lorentzian fit. The higher FWHM values when using a 442 nm excitation wavelength is explained by the higher incident laser power. Previous Raman spectroscopy studies on MoS₂ shows the same trend, explained by enhanced thermal effects^{5,26}.

In order to electrically probe an exfoliated MoSe₂ flake, we select a single terrace with uniform thickness to define the active region of the field-effect transistor. Electron-beam lithography (EBL) combined with reactive ion etching using Cl₂ are then used to define the device active region. The metal contacts are defined by a second EBL step followed by 80 nm-thick Ni evaporation and lift off. The highly doped Si substrate serves as back-gate for the MoSe₂ FETs. Several two- and four-point back-gated field effect transistors (FET) were investigated in this study.

The output and transfer characteristics of an FET fabricated on a 5.8 nm thick MoSe₂ flake (~ 8 layers), with channel length $L = 1.8 \mu\text{m}$ and width $W = 0.8 \mu\text{m}$ are shown in Fig. 2. The measurements presented in this paper are carried out in vacuum (~10⁻⁷ torr), and in dark. In each measurement the source contact is grounded, while the drain is biased. Figure 2(a) shows transfer characteristics defined as drain current (I_D) vs. drain voltage (V_D) measured at various back gate voltages (V_G) at room temperature. The I_D - V_D dependence is mostly linear, and does not show saturation at high drain bias, in contrast to what is expected in a conventional FET. Moreover the I_D - V_D data exhibit a slight super-linear behavior at low drain bias, which

suggests that the electrons are injected through a Schottky barrier at metal (Ni)-semiconductor interface. Figure 2(b) shows the transfer characteristic (I_D - V_G) measured at two different drain biases $V_D = 50 \text{ mV}$ and $V_D = 1 \text{ V}$. The device shows an n -type behavior, and is depleted from free carriers for $V_G < 0 \text{ V}$. The threshold voltage of this device, $V_T \cong 0 \text{ V}$ does not appear to change noticeably with V_D , consistent with a long-channel device. The I_{on}/I_{off} ratio at $V_D = 1 \text{ V}$ curve is larger than 10⁶, similar to reported On/Off ratio values for MoS₂, WS₂, and WSe₂ devices^{8,15,16}, and explained by the large energy gaps that characterize this family of materials.

To further probe the electron injection in MoSe₂, in Fig. 3 we show two sets of output characteristics measured on the same two-point back-gated MoSe₂ FET, but using a different source contact in each data set. For the same V_G value, different I_D values are obtained depending on which physical contact is used as source. This asymmetry in I_D - V_D data further confirms the presence of a Schottky barrier at the metal-semiconductor contact. As a result the electron injection depends not only to the device geometry, e.g. contact area, but also on the electric field across the metal/MoSe₂ interface, and therefore will be sensitive to MoSe₂ flake thickness, SiO₂ dielectric thickness, as well as gate and drain bias. Schottky barrier contacts are common place for other nano-electronic devices, such as carbon nanotube (CNT)²⁷ and nanowire devices²⁸. The presence of non-ohmic contacts affects adversely the device performance by reducing the On state current and prevents a quantitative analysis of the device characteristics. Most importantly, extracting the intrinsic MoSe₂ mobility from data such as that of Fig. 2 is difficult.

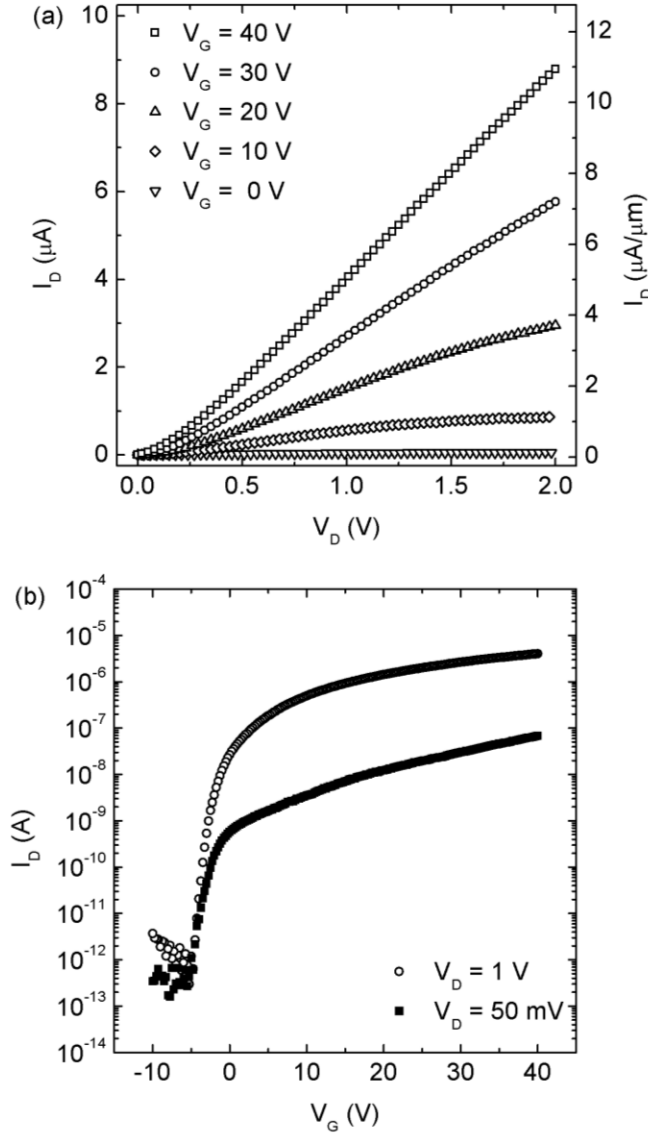


Fig. 2. (a) I_D vs. V_D measured at different V_G values. The data show a super-linear behavior at low V_D suggesting the presence of a Schottky barrier at the metal MoSe₂ contact. (b) I_D vs. V_G traces measured at $V_D = 50$ mV (solid squares), and $V_D = 1$ V (open circles) with $I_{on}/I_{off} > 10^6$ at $V_D = 1$ V.

To probe the intrinsic mobility of MoSe₂ flakes, we fabricate four-point back-gated devices, which allow conductivity measurements without contributions from the contact resistance of the metal-semiconductor Schottky barriers. The inset of Fig. 4 (a) shows an AFM image of a four-point MoSe₂ device. The outer contacts labeled *S* and *D* serve as source and drain, respectively. The inner contacts (V_1 , V_2) are used as voltage probes, and have a limited overlap with the MoSe₂ flake to minimize screening of the gate-induced charge density in the channel. The measured channel conductance (G) is defined as $G = I_D/(V_1 - V_2)$. Figure 4(a) shows the G vs. V_G data measured at different T values from 298 to 78 K. For V_G values lower than a threshold voltage (V_T), G remains vanishing. Above threshold, the G increases with V_G , with an approximately linear dependence. As the temperature is reduced, V_T shifts progressively towards higher voltages.

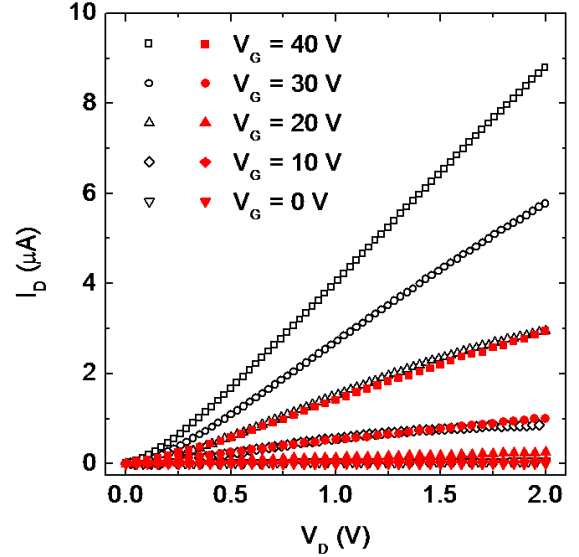


Fig. 3. (color online) Different I_D - V_D data sets obtained by swapping drain and source contacts on the same device. The asymmetry of the I_D values when swapping the S and D contacts is characteristic of FETs with Schottky contacts.

To offset the V_T shift with T , Fig. 4(b) shows G vs. $V_G - V_T$ at different T values. Figure 4(b) data show a noticeable increase of the $dG/d(V_G - V_T)$ slope with decreasing T . The intrinsic mobility can be thus extracted as $\mu = (L/W) \cdot dG/dV_G \cdot C_{ox}^{-1}$, where $C_{ox} = 1.2 \times 10^{-8}$ F·cm⁻² is the capacitance of the 285 nm-thick bottom SiO₂ dielectric; L and W denote the length and width of the active device area, respectively. The inset of Fig. 4 (b) shows the mobility dependence on temperature for three different devices. The room temperature mobility is as high as 50 cm²/V·s, and increases almost four fold when reducing the temperature to 78 K. In two dimensions, charged impurity scattering causes a temperature independent mobility in the degenerate limit, as in the case of graphene²⁹, and a $\mu \propto T$ dependence for a non-degenerate two-dimensional electron system. Acoustic phonon scattering generates a $\mu \propto T^{-1}$ dependence, and optical phonon scattering, including polar optical phonons, cause a stronger T -dependence in TMDs³⁰. A functional fit of the form $\mu^{-1}(T) = A + BT^v$ to the μ vs. T data of Fig. 4(b) inset yields an exponent $v=2.1$ for the highest mobility sample, suggesting that phonon scattering dominates in this sample. Temperature dependent Hall mobility measurements carried out on bulk MoSe₂ samples also report an increased mobility with reducing temperature.³¹

Lastly we address the contact resistance in our devices. Having measured the MoSe₂ resistivity using four-point devices, we can subtract the flake intrinsic resistance from the measured source-to-drain resistance in order to estimate the contact resistance. The room temperature contact resistance values range between 200 kΩ at large, $V_G - V_T = 35$ V gate overdrive, and increase to 6 MΩ as V_G approaches V_T . Reducing the temperature leads to an increase in contact resistance. The strong V_G dependence of the contact resistance provides further evidence for the presence of a Schottky barrier at the metal/MoSe₂ interface, an obstacle which will have to be overcome in order to increase the On current.

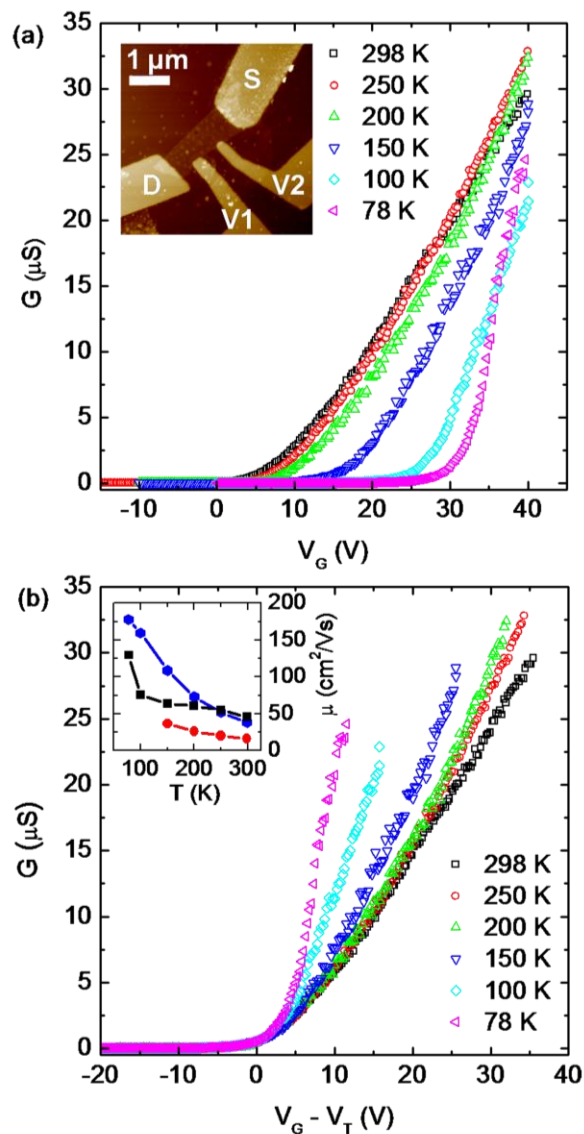


Fig. 4.(color online) (a) G vs. V_G at different temperatures, ranging from 298 to 78 K. The data shows a linear dependence above threshold, combined with a V_T shift towards higher voltages when reducing T . Inset: AFM image of a four-point device. The source (S), drain (D), and voltage probes (V_1 , V_2) are marked accordingly. (b) G vs. $V_G - V_T$ data for the same set of temperatures. Inset: μ vs. T for three different MoSe_2 devices.

In summary, we demonstrate n -type field-effect transistors on ultra-thin MoSe_2 flakes, showing high I_{on}/I_{off} ratios. We probe the intrinsic mobility as a function of temperature using gated four-point device structures, and show that the mobility increases significantly with lowering the temperature, which suggest phonon scattering plays a dominant role at room temperature.

This work is supported by ONR and Intel. We thank R. Pillarisetty for discussions.

- ¹ J.A. Wilson and A.D. Yoffe, *Adv. Phys.* **18**, 193 (1969).
- ² C. Ataca and S. Ciraci, *J. Phys. Chem. C* **116**, 8983 (2012).
- ³ K.S. Novoselov, D. Jiang, F. Schedin, T.J. Booth, V.V. Khotkevich, S.V. Morozov, and a K. Geim, *Proc. Natl. Acad. Sci.U.S.A.* **102**, 10451 (2005).

- ⁴ M.M. Benameur, B. Radisavljevic, J.S. Héron, S. Sahoo, H. Berger, and a Kis, *Nanotechnology* **22**, 125706 (2011).
- ⁵ D.J. Late, B. Liu, H.S.S.R. Matte, C.N.R. Rao, and V.P. Dravid, *Adv. Funct. Mater.* **22**, 1894 (2012).
- ⁶ H. Li, G. Lu, Z. Yin, Q. He, H. Li, Q. Zhang, and H. Zhang, *Small* **8**, 682 (2012).
- ⁷ K.S. Novoselov, a K. Geim, S.V. Morozov, D. Jiang, Y. Zhang, S.V. Dubonos, I.V. Grigorieva, and a a Firsov, *Science* **306**, 666 (2004).
- ⁸ B. Radisavljevic, a Radenovic, J. Brivio, V. Giacometti, and a Kis, *Nat. Nanotechnol.* **6**, 147 (2011).
- ⁹ H. Liu and P.D. Ye, *IEEE Electron Device Lett.* **33**, 546 (2012).
- ¹⁰ H.S. Lee, S.-W. Min, Y.-G. Chang, M.K. Park, T. Nam, H. Kim, J.H. Kim, S. Ryu, and S. Im, *Nano Lett.* **12**, 3695 (2012).
- ¹¹ H. Li, Z. Yin, Q. He, H. Li, X. Huang, G. Lu, D. Wen, H. Fam, A. Iing, Y. Tok, Q. Zhang, and H. Zhang, *Small* **8**, 63 (2012).
- ¹² B. Radisavljevic, M.B. Whitwick, and A. Kis, *ACS Nano* **5**, 9934 (2011).
- ¹³ B. Radisavljevic, M.B. Whitwick, and A. Kis, *Appl. Phys. Lett.* **101**, 043103 (2012).
- ¹⁴ H. Wang, L. Yu, Y.-H. Lee, Y. Shi, A. Hsu, M.L. Chin, L.-J. Li, M. Dubey, J. Kong, and T. Palacios, *Nano Lett.* **12**, 4674 (2012).
- ¹⁵ H. Fang, S. Chuang, T.C. Chang, K. Takei, T. Takahashi, and A. Javey, *Nano Lett.* **12**, 3788 (2012).
- ¹⁶ W. Sik Hwang, M. Remskar, R. Yan, V. Protasenko, K. Tahy, S. Doo Chae, P. Zhao, A. Konar, H. (Grace) Xing, A. Seabaugh, and D. Jena, *Appl. Phys. Lett.* **101**, 013107 (2012).
- ¹⁷ A. Jaeger-Waldau, M.C. Lux-Steiner, R. Jaeger-Waldau, and E. Bucher, *Springer Proc. Phys.* **54**, 397 (1991).
- ¹⁸ S. Tongay, J. Zhou, C. Ataca, K. Lo, T.S. Matthews, J. Li, J.C. Grossman, and J. Wu, *Nano Lett.* ASAP, (2012).
- ¹⁹ W.S. Yun, S. Han, S.C. Hong, I.G. Kim, and J. Lee, *Phys. Rev. B* **85**, 1 (2012).
- ²⁰ J. M. Ukrainkii and A. B. Novoselova, *Dokl. Chem. Nauk SRRR* **139**, 1136 (1961).
- ²¹ R.A. de G. and A.W. R. Coehoorn, C. Haas, J. Dijkstra, C. J. F. Flipse, *Phys. Rev. B* **35**, 6195 (1987).
- ²² R. Bissessur and H. Xu, *Mat. Chem. Phys.* **117**, 335 (2009).
- ²³ R.D. and C.N.R.R. H. S. S. Ramakrishna Matte, Blake Plowman, *Dalton Trans.* **40**, (2011).
- ²⁴ T. Sekine, M. Izumi, T. Nakashizu, K.Uchinokura, and E. Matsuura, *J. Phys. Soc. Jpn.* **49**, 1069 (1980).
- ²⁵ R. He, Z. Wang, R.L.J. Qiu, C. Delaney, B. Beck, T.E. Kidd, C.C. Chancey, and X.P. a Gao, *Nanotechnology* **23**, 455703 (2012).
- ²⁶ S. Najmaei, Z. Liu, P.M. Ajayan, and J. Lou, *Appl. Phys. Lett.* **100**, 013106 (2012).
- ²⁷ P. Avouris, J. Appenzeller, R. Martel, S.J. Wind, and S. Member, *Proc. IEEE* **91**, 1772 (2003).
- ²⁸ E. Liu, N. Jain, K.M. Varahramyan, S. Member, J. Nah, S.K. Banerjee, and E. Tutuc, *IEEE Trans. Nanotechnol.* **9**, 237 (2010).
- ²⁹ J.-H. Chen, C. Jang, S. Xiao, M. Ishigami, and M.S. Fuhrer, *Nat. Nanotechnol.* **3**, 206 (2008).
- ³⁰ K. Kaasbjerg, K. Thygesen, and K. Jacobsen, *Phys. Rev. B* **85**, 115317 (2012).
- ³¹ R. Fivaz and E. Mooser, *Phys. Rev.* **163**, 743 (1967).